Development of composite steam electrodes for electrolysers based on barium zirconate

Nuria Bausá[1], Cecilia Solís[1], Ragnar Strandbakke[2], José M. Serra[1,]*

1: Instituto de Tecnología Química (Universidad Politécnica de Valencia – Consejo Superior de Investigaciones Científicas), Av. Naranjos s/n, E-46022 Valencia (SPAIN)
2: Department of Chemistry, University of Oslo, FERMiO, Gaustadalléen 21, NO-0349 Oslo, Norway.

* to whom correspondence should be addressed, Fax 0034.963.877.809

e-mail: jmserra@itq.upv.es

ABSTRACT:

$La_{0.6}Sr_{0.4}Co_{0.2}Fe_{0.8}O_{3-\delta}$ (LSCF), $La_2NiO_{4+\delta}$ (LNO), $La_{0.87}Sr_{0.13}CrO_4$ (LSC), $La_{0.8}Sr_{0.2}MnO_{3-\delta}$ (LSM) and $Ba_{0.5}Sr_{0.5}Co_{0.8}Fe_{0.2}O_{3-\delta}$ (BSCF) composite anodes deposited on proton-conducting $BaCe_{0.2}Zr_{0.7}Y_{0.1}O_{3-\delta}$ (BCZY27) electrolytes were studied as steam electrolysis anodes in symmetric cells. The effect of the electrode composition and microstructure on the electrochemical behavior was investigated using impedance spectroscopy in the 800-500 ºC range under 3 bar of pressure of wet air (75% of steam). The first screening revealed that 50-50 (vol.%) LSCF/BCZY27 composite anodes show the best performance, reaching polarization resistances < 0.68 $\Omega \cdot cm^2$ at 700 °C and high steam pressure (0.75 bar of air and 2.25 bar of steam). The performance of the LSCF/BCZY27 composite was further improved by changing the ratio of the different phases. Finally the anode operation conditions (steam, oxygen and total pressures) were systematically varied in order to identify and characterize the different electrochemical processes that take place in the anode under realistic operation.

KEYWORDS:

PCEC; high steam pressure; proton conductor; anode; LSCF; composite

1. Introduction

Proton conducting ceramics have attracted much interest due to their applications in energy conversion, as protonic conducting -solid oxide- fuel cells (PCFC), electrolysers (PCEC), hydrogen sensing, hydrogen separation and chemicals synthesis.[1-6] Among all the protonic conducting ceramics barium cerates and zirconates have demonstrate promising properties.[7] Barium cerates based materials show the highest protonic conductivity values, but they are unstable under CO_2 containing atmospheres, which restricts their practical application. Barium zirconates based compounds are more stable, but present a much lower protonic conductivity due to the high grain boundary resistivity.[8] In order to find the optimal mix between chemical stability and proton conductivity, $BaCe_{1-x-y}Zr_xY_yO_{3-\delta}$ (BCZY) materials have been proposed as proton conducting electrolytes, although they present lower protonic conductivity compared to the cerates. The search for new steam- or air electrode materials compatible with BCZY for PCEC operation is challenging since the electrode should exhibit (i) tailored electronic and ionic (protonic and oxygen-ion) conductivity, (ii) proper microstructure for fast gas exchange, and (iii) thermo-chemical stability in air and high-steam gas environments at high temperature.

High temperature electrolysis (HTE) of steam offers high efficiency of conversion of renewable and peak electricity into hydrogen[9, 10]. In solid oxide electrolysers (SOECs)[11, 12], that use oxide ion conducting electrolytes and operate at around 800 °C, hydrogen is produced on the steam feed side (nickel-based electrode). As a consequence, SOECs present two drawbacks, i.e., the production of very humid hydrogen and the risk of oxidation of the metallic electrode at high-steam concentrations. On the other hand, in proton conducting electrolysers (PCECs)[13-15] a high temperature proton conducting electrolyte is used instead and protons are pumped and form dry H_2, leaving O_2 on the steam side. These PCECs can produce pressurised dry H_2 directly on the cathode (nickel-based electrode). In PCECs, steam is fed in the air/oxygen electrode (anode), typically made of mixed ionic-electronic conducting ceramics.

In the present work, different materials have been proposed as electrodes for BCZY based PCECs, comprising mixed ionic-electronic conductors as $La_{0.6}Sr_{0.4}Co_{0.2}Fe_{0.8}O_{3-\delta}$ (LSCF)[16, 17] and $Ba_{0.5}Sr_{0.5}Co_{0.8}Fe_{0.2}O_{3-\delta}$ (BSCF)[17] and various $LaMO_x$ materials [18]

2. Experimental

$BaCe_{0.2}Zr_{0.7}Y_{0.1}O_{3-\delta}$ (BCZY27) powder (CerpoTech) was calcined at 1100 ºC for 6 h and ball-milled for 10 h in acetone. $Ba_{0.5}Sr_{0.5}Co_{0.8}Fe_{0.2}O_{3-\delta}$ (BSCF) was provided by IKTS Fraunhofer, $La_2NiO_{4+\delta}$ (LNO) by CerpoTech, $La_{0.87}Sr_{0.13}CrO_4$ (LSC) by Praxair and $La_{0.8}Sr_{0.2}MnO_{3-\delta}$ (LSM) by Fuel Cell Materials. $La_{0.6}Sr_{0.4}Co_{0.2}Fe_{0.8}O_{3-\delta}$ (LSCF) was prepared by the Pechini synthesis method.

Chemical compatibility of the different electrode materials was tested by using X-ray diffraction (XRD) analysis of different mixtures: LSM, LNO and LSC after sintering together with BCZY27 at 1100 ºC for 2 h and LSFC and BSFC after sintering with BCZY27 at 1000 ºC for 2 h. XRD patterns were recorded in the 2θ range from 20 to 70º on a CubiX FAST equipment using CuKα$_{1,2}$ radiation and an X'Celerator detector in Bragg-Brentano geometry and patterns were analyzed using X'PertHighscore Plus software (PANalytical).

The microstructure was investigated using a field emission scanning electron microscopy (FE-SEM) (Zeiss Ultra 55), and the elemental analysis was carried out with energy-dispersive X-ray spectroscopy (EDS) (INCA, Oxford).

Commercial BCZY27 CerpoTech powder was used to prepare the electrolytes. Dense ~1 mm-thick BCZY disks were obtained by uniaxially pressing the powder at approximately 120 MPa and firing at 1550 °C for 12 h.

Cer-cer composites of the electrolyte and the different selected electrode materials were prepared by mixing 50 vol. % of each phase and milling them together in an agate mortar. Inks for screen printing were prepared by using terpineol and ethylcellulose (10%) in a roller mixer. Porous 30µm-thick electrodes were obtained by screen printing the inks on both sides of the BCZY27 electrolyte. The sintering temperature of the electrodes was 1100 ºC for LSM/BCZY27 and 1000 ºC for LSCF/BCZY27 and BSCF/BCZY27. The final symmetric button cell was 14.5 mm in diameter while the anodes were 9 mm in diameter approximately.

Finally, one LSCF/BCZY27 cer-cer electrode was optimized by changing the volumetric ratio of LSCF and BCZY27. Electrochemical performance of the different electrodes was investigated by preparing symmetric cells and by performing

electrochemical impedance spectroscopy (EIS) measurements in a two-point/four wire configuration with platinum current collector meshes. Input signal was 0 V DC – 20 mV AC in the $0.03 - 1 \cdot 10^6$ Hz frequency range (Autolab PGSTAT204 and PGSTAT128N potentiostats both equipped with a FRA32M module for impedance analysis). Raw impedance data were fitted to an equivalent circuit using Z-plot software. Electrode polarization resistances were measured from 800 ºC to 500 ºC under a total pressure of 3 bar (75% steam in air). The pressure dependency on polarization resistance was investigated by varying the total pressure with constant oxygen to steam ratio (75 % steam, 25 % O_2) and by varying pO_2 or pH_2O and allowing total pressure to vary proportionally. The flow was always kept constant at 100 mL·min^{-1}.

3. Results and discussion

The chemical compatibility of the different selected electrode materials and the BCZY27 electrolyte was tested by means of XRD upon heat treatment. Figure 1 shows the XRD patterns of the LSM (a), LNO (b) and LSC (b) after sintering together with BCZY27 at 1100 ºC for 2 h and the LSFC (c) and BSCF (d) after sintering with BCZY27 at 1000 ºC for 2 h. Furthermore, different reference patterns and starting material patterns are also included for comparison. It can be observed that while LSM, LSCF and BSCF are stable, with no extra peaks after the sintering process, LNO and LSC present some extra peaks as a result of reaction with the BCZY27 electrolyte phase. LNO gives rise to Ce_6O_{11} and/or BaO segregation, while LSC favors the formation of $BaCrO_4$. Thus, only LSM, LSCF and BSFC were further investigated in this study.
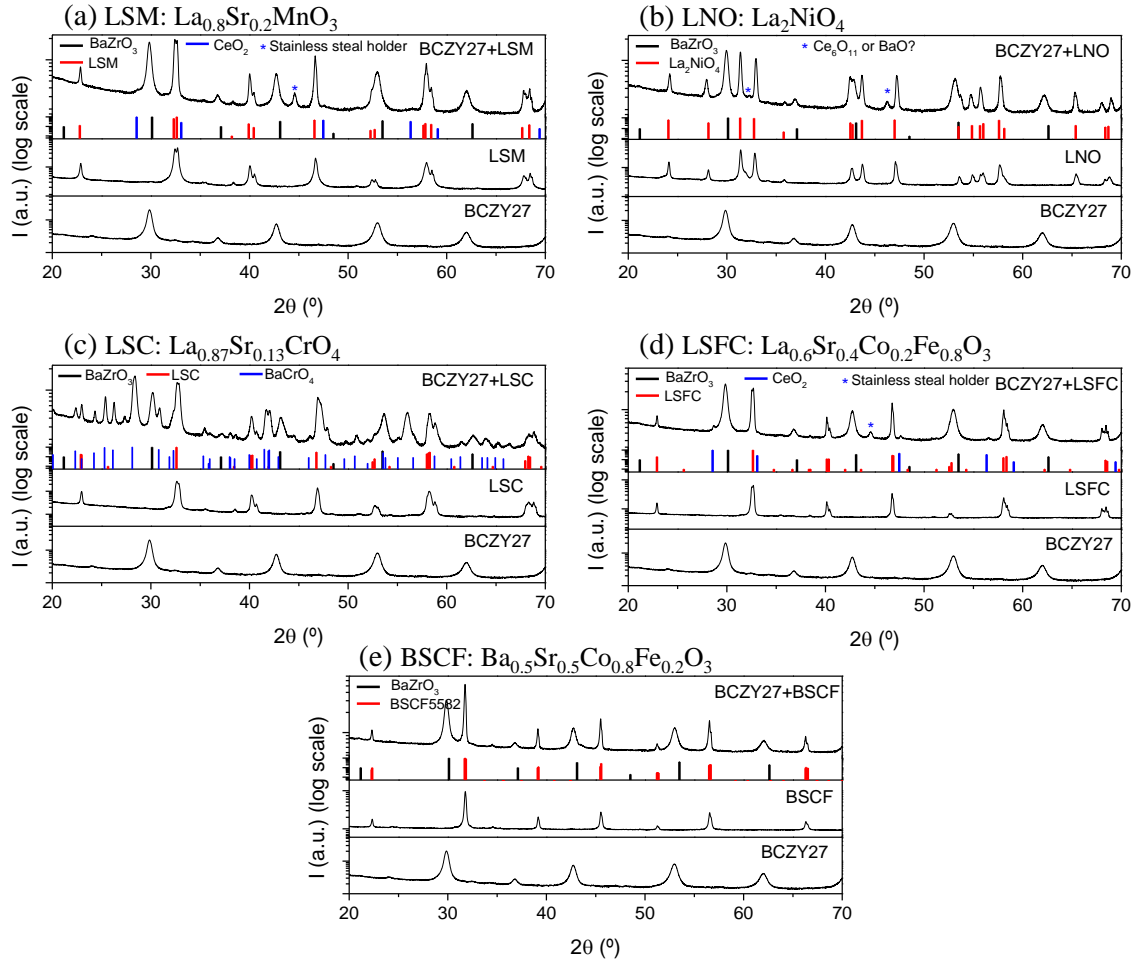
Figure 1. XRD patterns of the (a) LSM, (b) LNO and (c) LSC after sintering with BCZY27 at 1100 ºC for 2 h and (d) LSFC and (e) BSFC after sintering with BCZY27 at 1000 ºC for 2 h.

The stability of BCZY27 with respect to LSM, LSFC and BSFC was also investigated under a total pressure of 3 bar, with a 25% air and / 75% (1.5 bar) of steam at 700 ºC for 72 h. XRD analysis (Figure 2) reveals that BSCF partially decomposed as can be deduced from the intensity decrease of the diffraction peaks and the appearance of some new phases (not identified). However, the other tested materials, i.e. BCZY27, LSM and LSFC, remained stable, with no extra diffraction peaks. There are slight changes in the diffraction peaks of LSCF, i.e., some double peaks becoming single and this is attributed to changes from orthorhombic to cubic symmetry. In summary, BCZY27, LSM and LSCF remained stable under electrolysis operation conditions, that is, high steam pressure, while the degradation of BSCF is expected under these conditions.
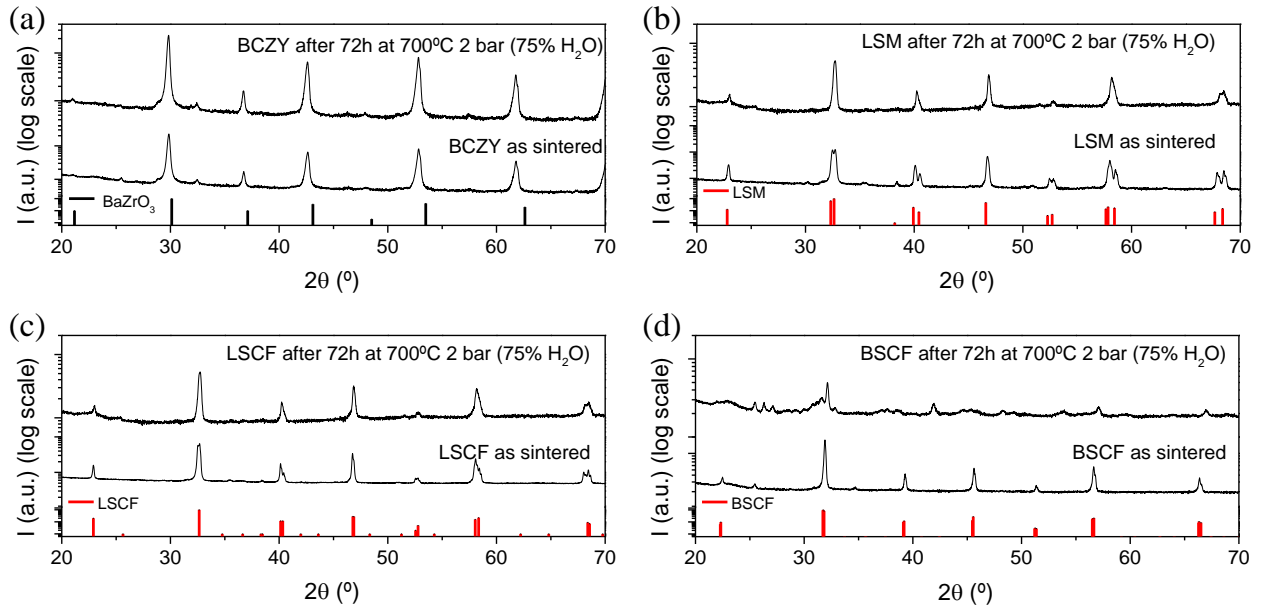
Figure 2. XRD patterns of the (a) BCZY27, (b) LSM, (c) LSCF and BSFC after being 72 h at 700 ºC under 3 bar of air with the 75% of steam (2.25 bar)

Polarization resistances (Rp) of the three composite electrodes at 0.75 bar of air and 2.25 bar of steam are represented as a function of temperature in Figure 3. The highest Rp is observed for BSCF/BCZY27 electrode and this ascribed to the degradation under operation conditions (as shown in figure 2d). The LSM/BCZY27 electrode shows a slightly better performance at high temperatures, although around 100 $\Omega\cdot cm^2$ at 600 ºC. R_p of LSCF/BCZY27 is by far the lowest of the three tested electrodes being 2 orders of magnitude lower than the one measured for other two, and reaching 0.1 $\Omega\cdot cm^2$ at 800 ºC.
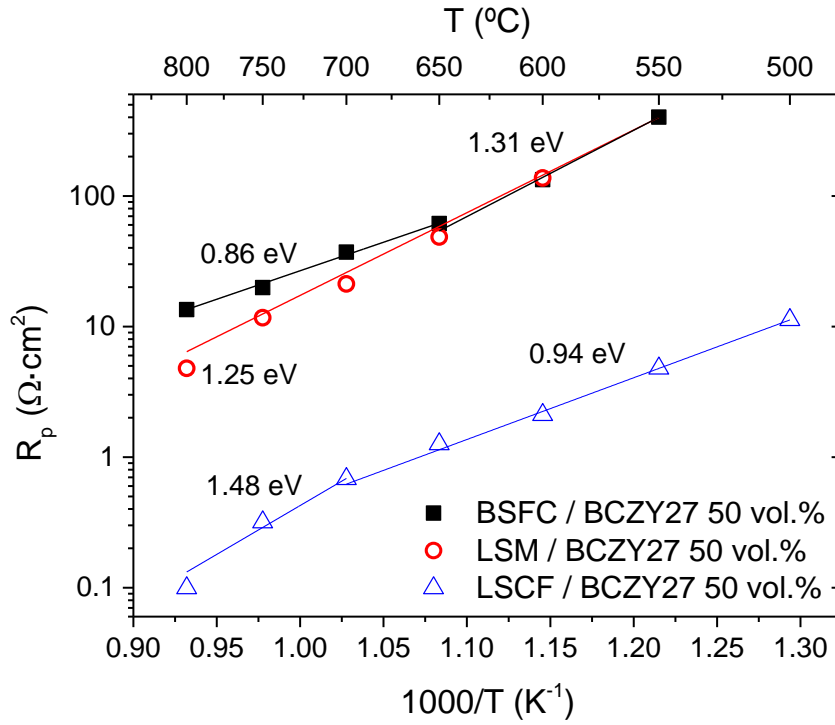
Figure 3. Temperature dependence of Rp for the three different tested electrodes

In order to identify the different mechanisms limiting the electrode operation and mostly contributing to R_p, impedance spectra were fitted by using equivalent circuits, slightly different for each type of electrode, which represent best the rate-limiting steps in each electrode. Specifically, The equivalent circuit $L(R_0Q_0)(R_{MF}Q_{MF})(R_{LF}Q_{LF})$ was employed for the LSCF/BCZY (inset in Figure 4), $L(R_0Q_0)(R_{HF}Q_{HF})(R_{LF}Q_{LF})$ for the LSM/BCZY electrode and the equivalent circuit $L(R_0Q_0)(R_{HF}Q_{HF})(R_{MF}Q_{MF})(R_{LF}Q_{LF})$ for the BSCF/BCZY electrode. (inset in the supporting information, Figure S1). Figure 4 shows an example of the overall fit of the obtained results for the LSFC/BCZY27 electrode measured at 750 ºC (circles are measured values, black line is fitting) and the different contributions to R_p. The different arcs were assigned to different reaction steps by the associated capacitance values (C) obtained from each arc and the frequency rates. The first arc, with associated capacitance $C_0 \sim 5 \times 10^{-9}$ F/cm^2 and that takes place in the frequency range from 500 kHz to 1 MHz, can be assigned to the electrolyte grain boundary[17] and does not contribute to the total Rp showed in Figure 3. Thus R_{MF} and R_{LF} are the electrode resistances, with associated capacitance of $C_{MF} \sim 1 \times 10^{-4}$ F/cm^2, which occurs at frequencies between 4 and 80 kHz and $C_{LF} \sim 4$ F/cm^2, in the frequency range between 1 and 30 Hz.

7

In general, for all the different tested electrodes the higher frequency (HF) semicircles can be assigned to a charge transfer reaction (e.g. transfer of protons between the electrolyte and the electrode), while the lower frequency (LF) semicircles, with higher associated capacitance values, can be ascribed to different elementary reactions on the surface, e.g., dissociative adsorption and diffusion of oxygen step.[16, 18-21]
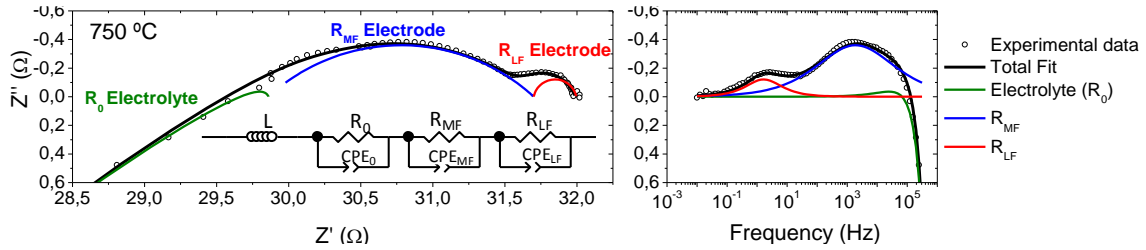

Figure 4. Impedance spectrum recorded for the LSCF/BCZY27 symmetric cell at 750 ºC in air (steam pressure 2.25 bar). The symbols correspond to the experimental data and the solid lines to the fit using the shown equivalent circuit.
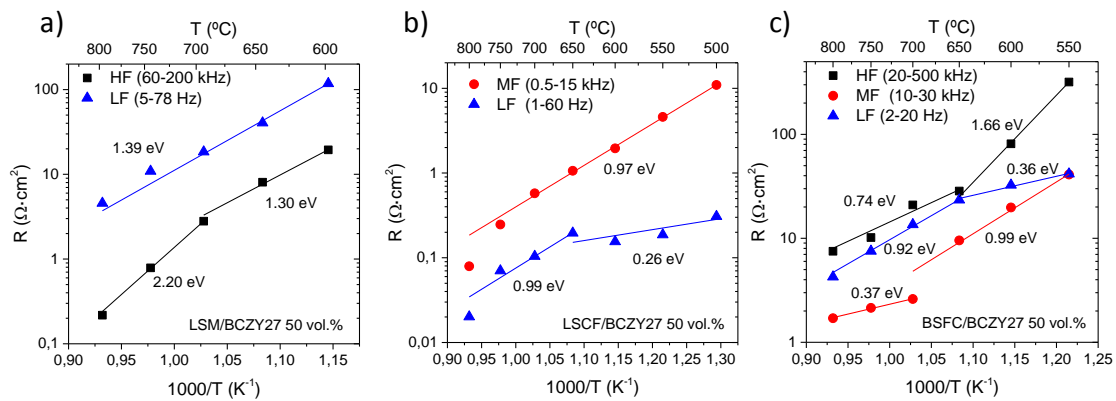

Figure 5. Temperature dependency of modelled resistances of LSM/BCZY27 50 vol.% (a), LSCF/BCZY27 50 vol.% (b) and BSCF/BCZY27 50 vol. % (c) symmetric cells measured at 3 bar, 75% of steam in air.

Figure 5 presents partial polarization resistances as a function of temperature for the three tested electrodes. LSM/BCZY27 electrode has three different contributions and it is limited by LF surface-associated processes in the whole temperature range, displaying an activation energy (E_A) value of 1.39 eV. The HF contribution, attributed to the charge transfer reaction, constitutes some 20 % of the total R_p and displays E_A values of 2.2 eV between 700 and 800 ºC and 1.3 eV between 500 and 700 ºC. This is well in line with previous reports based on LSM-composites on both protonic and oxide-ion conducting electrodes[5, 22, 23] although these values are significantly higher than those related to limiting process solely involving protons, e.g. $E_A \leq 0.6$ eV.

Therefore, this electrode appears to be limited by a surface process, impeded by the limited oxygen activation and water splitting electrocatalytic activity of LSM [24, 25]. The activation energy of the rate determining LF process is in relatively good agreement with literature values.[26-29].

The LSCF/BCZY27 electrode performance is limited by contributions appearing at MF, especially at temperatures 650ºC. The LF process is not rate limiting and R_{LF} is about twice lower than the MF resistance, although a change in the activation energy of the LF contribution is observed, which can be related to a change in the prevailing conduction mechanism in BCZY27 from oxide-ionic (high temperature) to protonic (lower temperature)[30, 31]. SEM analysis (Figure 6) of tested-cells cross-sections reveals that the electrode thickness is around 30-40 µm and the microstructure is highly porous. In the left-hand images of the three different cells, the interface between the composite electrode and the electrolyte of the symmetric cell is visible whereas in the following pictures the composite porous electrode can be observed at high magnification.
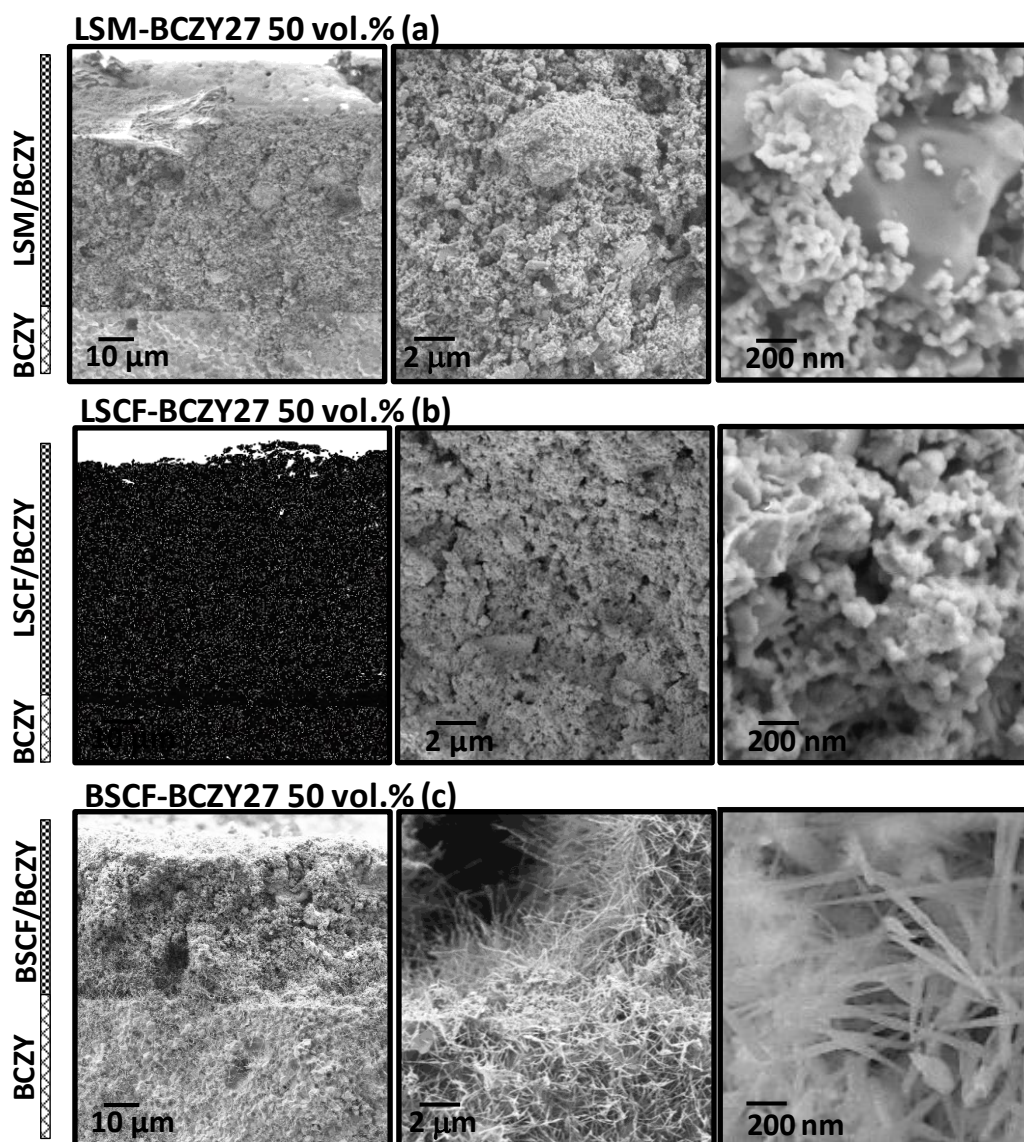
Figure 6. SEM micrographs of the fractured cross-section of LSM/BCZY27 (a), LSCF/BCZY27 (b) and BSCF/BCZY27 (c)

In the images of the LSM/BCZY27 electrode (Figure 6a right-hand), the different components of the composite can be distinguished at higher magnification and the larger particles in the composite correspond to LSM. In LSCF/BCZY27 electrode (Figure 6b), the particle size of the two phases in the porous composite is very similar and thus the microstructure is optimized. In the case of BSCF/BCZY27 electrode, the exposure to steam causes the decomposition of the electrode material and formation of Ba-rich needle-like crystals all over the electrode surface (Figure 6 c).

The variation of vol. ratio of the different phases in the composite was studied for the best tested electrode, i.e. the LSCF/BCZY27 composite. Figure 7a shows the temperature dependence of R_p for three different electrodes with different phase

10

compositions, LSCF/BCZY27 40/60, 50/50 and 60/40 vol. % composites. The behavior of the three electrodes is similar and the best performance is observed for the 50/50 vol. % composite, as can be seen in Figure 7b where R_p at 700 ºC is plotted as a function of the vol.% of BCZY27 phase. Furthermore, this plot also shows the LF and MF resistance contributions and confirms that the MF process determine the electrode performance regardless of the BCZY27 vol. %.
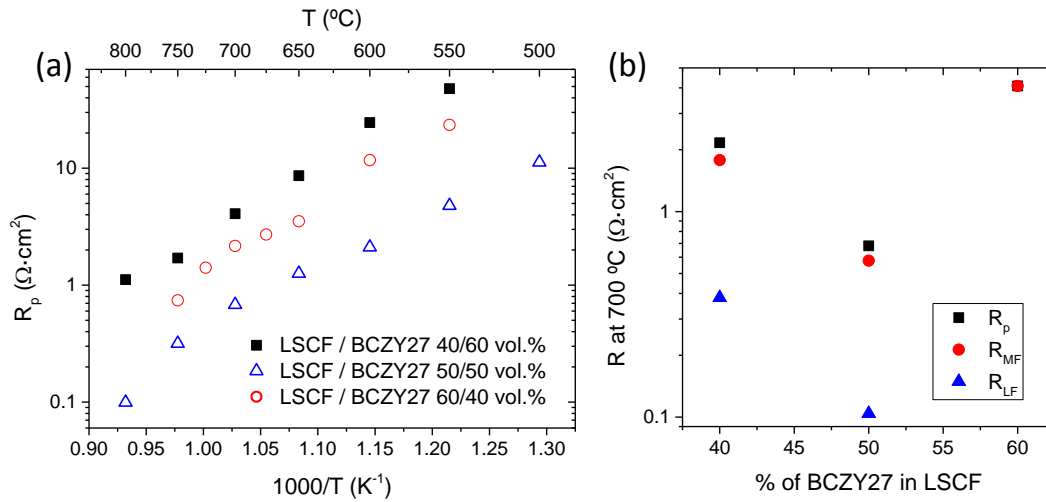

Figure 7. (a) Temperature dependence of R_p for different tested electrodes with different phase compositions; and (b) R_p and R_{LF} and R_{MF} contributions measured at 700 ºC as a function of the vol% of BCZY protonic phase introduced in the LSCF electrode

In order to further study the nature of the different resistance contributions, the best performing electrode (LSCF/BCZY27 50/50) (Figure 8) and the BCZY27 electrolyte material (Figure 9) were measured under different total pressures (p_{total}) and different pO$_2$ and pH$_2$O pressures (Figure 9). All data were obtained from the corresponding impedance spectra, i.e., electrode contributions values were obtained from the impedance fitting (arcs) and the electrolyte contribution from the cut with the x-axis. Figure 8a shows total and partial R_p as a function of the total pressure, when it changes from 1 to 6 bar, with a constant composition of steam (75%) and air (25%), thus both pH$_2$O and pO$_2$ vary proportionally (see the pH$_2$O variation in the secondary top y-axis, that goes from 1.5 to 4.5 bar). While the LF resistance slightly increases until reaching a plateau, the MF resistance decreases linearly with increasing total pressure together with pH$_2$O. The corresponding EIS spectra can be observed in Figure S2 in Supporting Information. Figure 9a depicts the BCZY27 electrolyte conductivity extracted from the same impedance spectra. The conductivity increases with the total pressure (and pO$_2$

11

and pH_2O), which can be ascribed to (i) higher proton conductivity, (ii) higher oxygen-ion conductivity and (iii) higher p-type electronic conductivity. It has previously been reported that BCZY27 exhibits p-type electronic and ionic carriers conduction at high temperatures and pO_2.[7, 32] Higher pO_2 gives rise to higher p-type and thus higher electrolyte conductivity and lower Rp. Indeed, Rp is both improved by higher pO_2 and apparently lowered by the electron-leaky current. In addition, higher pH_2O leads to higher total (proton) conductivity and possibly also a lower Rp. Thus the decrease of R_p with increasing total pressure can be ascribed to the increased p-type conduction induced by the higher pO_2.
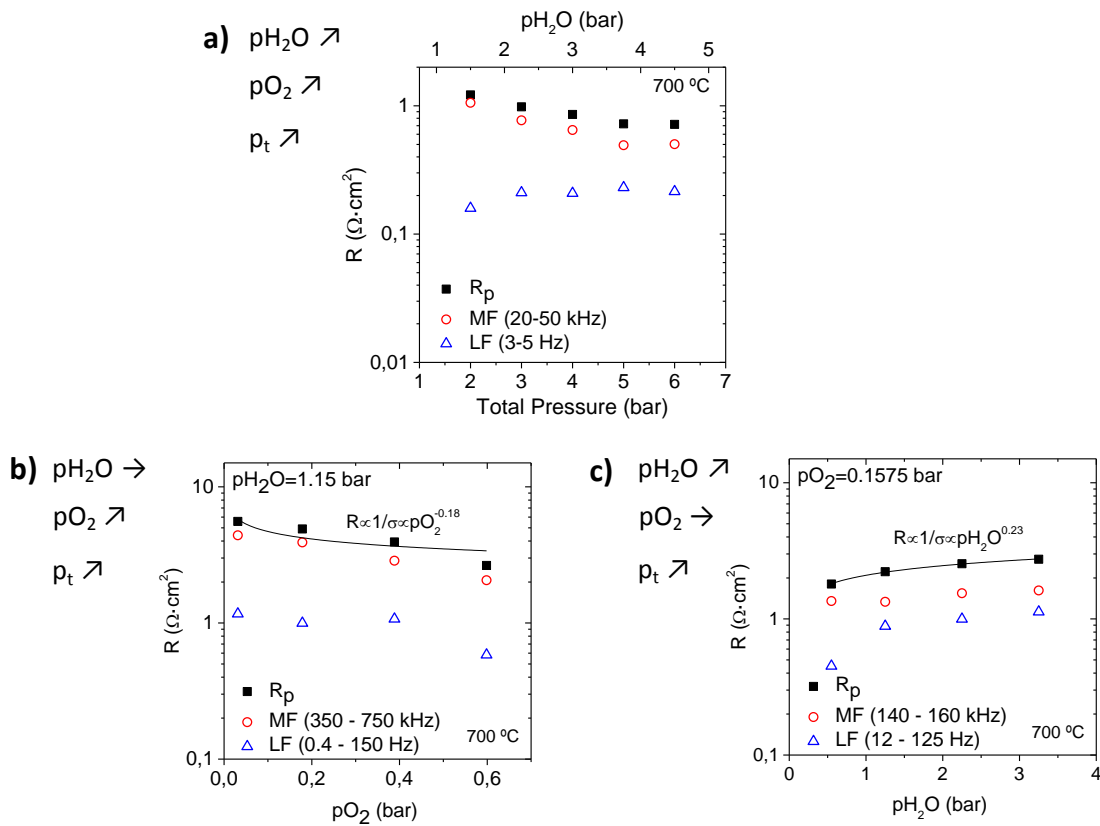

Figure 8. R_p and MF and LF contributions at 700 ºC as a function of: (a) total pressure with a constant (75%) steam concentration (the total steam variation is also showed in the secondary top y-axis); (b) pO_2 at constant pH_2O ~1.15 bar; and (c) pH_2O at constant pO_2 ~0.1575 bar

Figure 8b represents the isothermal analysis of R_p, and the HF and MF resistance contributions as a function of pO_2 at constant pH_2O ~1.15 bar (thus the total pressure also increases). R_p and all the different contributions decrease with increasing pO_2 following a power law, $R_p \propto pO_2^{-0.18}$. The corresponding conductivity of BCZY27 electrolyte (Figure 9b) increases with increasing pO_2 following a power law, $\sigma \propto pO_2^{0.016}$. This small exponent is in contrast with the expected values $(^1/_6 - ^1/_4)$ for p-type

12

electronic conductor and reflects the importance of the ionic transport in this electrolyte under these oxidizing conditions.

Figure 8c represents R_p and the HF and MF contributions as a function of pH$_2$O at constant pO$_2$ ~0.1575 bar. It can be observed that R_p and both HF and MF contributions increase with pH$_2$O following a power law, $R_p \propto pH_2O^{0.23}$. This can be related to the fact that (1) p-type conduction is lowered and the R_p is gradually less short-circuited by electron-leak current; and (2) the higher water gas concentration and surface coverage on the electrode impedes desorption and out-diffusion of the form O$_2$ molecules. The corresponding conductivity of the electrolyte (Figure 9c) reveals a pH$_2$O dependency following $\sigma \propto pH_2O^{0.043}$, significantly smaller than the expected $pH_2O^{0.5}$, that accounts for the hydration equilibrium, as the ideal behavior of a pure proton conductor. This smaller pH$_2$O dependency can be related to possible processes (i) BCZY27 hydration starts approaching a saturation limit at pH$_2$O > 1 bar and (ii) the decline in p-type conduction as a consequence of the proton incorporation (oxide hydration) that involves the consumption of electron holes.
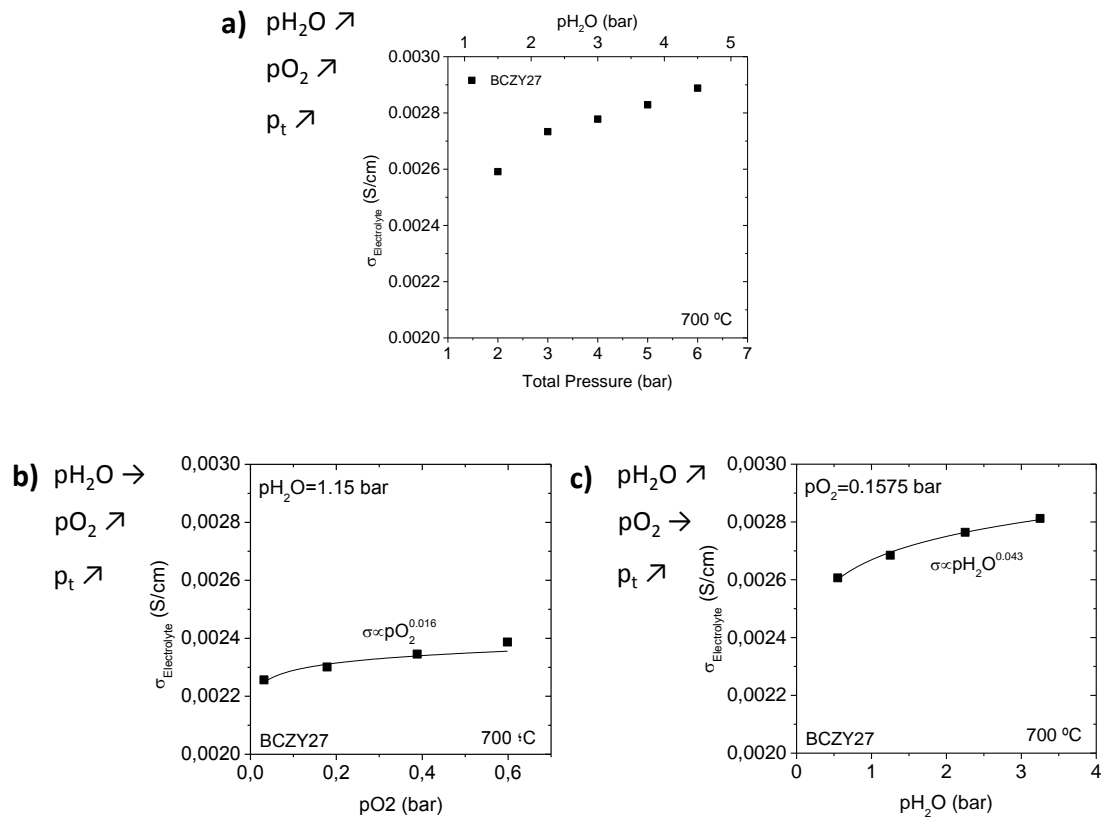

Figure 9. Total conductivity of the BCZY27 electrolyte as a function of: (a) total pressure at constant (75%) steam concentration (the total steam variation is also showed in the top y-axis); (b) pO$_2$ at constant pH$_2$O ~1.15 bar (c); and pH$_2$O at constant pO$_2$ ~0.5 bar

4. Conclusions

Five perovskite materials LSCF, LNO, LSC, LSM and BSCF were considered as potential steam electrodes for BCZY27 electrolysers. LSC and LNO were not compatible and react with BCZY27 electrolyte during electrode firing. LSCF and LSM remained stable under electrolysis conditions (3 bar, 25% air, 75% steam) while BSCF degraded to form Ba-rich needle-like phases.

Different ceramic-ceramic (cer-cer) composite electrodes were prepared by mixing 50 vol.% of BSCF, LSCF and LSM materials and 50 vol.% of BCZY27. These electrodes were tested as anodes on symmetric BCZY27 button cells in the temperature range 500-800 °C under electrolysis conditions.

The LSCF/BCZY27 composition was varied and the best performance is observed for the electrode with 50/50 vol. ratio, reaching polarization resistances < 0.68 $\Omega \cdot cm^2$ at 700 °C. The effect of both $p H_2O$ (0.4 - 3.2 bar) and $p O_2$ (0.05 − 0.6 bar) was studied on the polarization resistance and BCZY27 conductivity. Increasing $p H_2O$ leads to a slight increase in the electrode polarization resistance (R_p) while increasing and $p O_2$ gives rise to a slight reduction in R_p. The electrolyte conductivity slightly increases with rising both $p H_2O$ and $p O_2$.
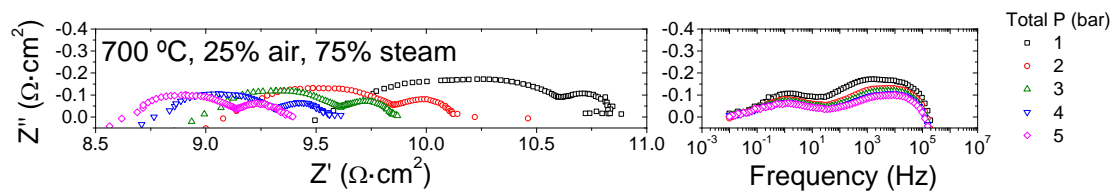
5. Acknowledgements

SUPPORTING INFORMATION
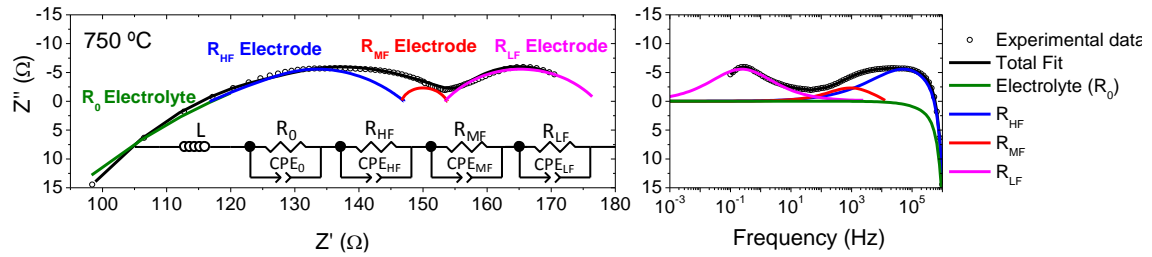
Supporting Figure S1: Impedance spectrum recorded for the BSCF/BCZY27 symmetric cell at 750 ºC in air (steam pressure 2.25 bar). The symbols correspond to the experimental data and the solid lines to the fit using the shown equivalent circuit.

Supporting Figure S2: EIS spectra as a function of the total pressure at constant concentrations: 75% of steam and 25% of air
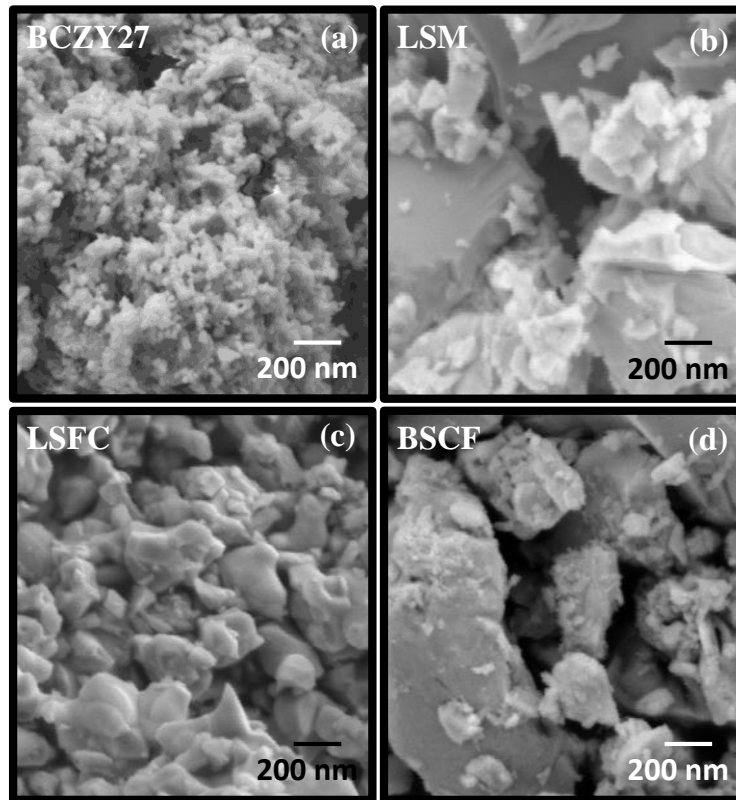
Supporting Figure S3: SEM micrographs of (a) BCZY27, (b) LSM, (c) LSFC and (d) BSCF materials used as starting powder for electrode preparation

The microstructure of the different powders used for the electrodes development can be observed in SEM images. The crystal size of the BCZY27 is very small (below 10 nm) and only comparable to that of the LSFC phase (of around 50 nm). However, LSM and BSCF present bigger particle sizes, between 200 and 600 nm.

REFERENCES

[1]   H. Iwahara, *Solid State Ionics* **77** (1995) (0) 289.

[2]   H. Iwahara, Y. Asakura, K. Katahira, M. Tanaka, *Solid State Ionics* **168** (2004) (3–4) 299.

[3]   S. Escolástico, C. Solís, J.M. Serra, *International Journal of Hydrogen Energy* **36** (2011) (18) 11946.

[4]   C. Solís, V.B. Vert, M. Fabuel, J.M. Serra, *Journal of Power Sources* **196** (2011) (22) 9220.

[5]   C. Solís, L. Navarrete, S. Roitsch, J.M. Serra, *Journal of Materials Chemistry* **22** (2012) (31) 16051.

[6]   S. Escolastico, C. Solis, C. Kjolseth, J.M. Serra, *Energy & Environmental Science* **7** (2014) (11) 3736.

[7]   S. Escolástico, M. Ivanova, C. Solís, S. Roitsch, W.A. Meulenberg, J.M. Serra, *RSC Advances* **2** (2012) (11) 4932.

[8]   Y. Yamazaki, R. Hernandez-Sanchez, S.M. Haile, *Chemistry of Materials* **21** (2009) (13) 2755.

[9]   C. Duan, J. Tong, M. Shang, S. Nikodemski, M. Sanders, S. Ricote, A. Almansoori, R. O'Hayre, *Science* **349** (2015) (6254) 1321.

[10]   L. Bi, S. Boulfrad, E. Traversa, *Chemical Society Reviews* **43** (2014) (24) 8255.

[11]   M. Ni, M.K.H. Leung, D.Y.C. Leung, *International Journal of Hydrogen Energy* **33** (2008) (9) 2337.

[12]   A. Brisse, J. Schefold, M. Zahid, *International Journal of Hydrogen Energy* **33** (2008) (20) 5375.

[13]   H. Iwahara, H. Uchida, N. Maeda, *Journal of Power Sources* **7** (1982) (3) 293.

[14]   K.D. Kreuer, *Solid State Ionics* **97** (1997) (1-4) 1.

[15]   E. Stefan, T. Norby, *Chemical Communications* **52** (2016) (9) 1759.

[16]   S. Ricote, N. Bonanos, P.M. Rorvik, C. Haavik, *Journal of Power Sources* **209** (2012) 172.

[17]   J. Dailly, S. Fourcade, A. Largeteau, F. Mauvy, J.C. Grenier, M. Marrony, *Electrochimica Acta* **55** (2010) (20) 5847.

[18]   S. Ricote, N. Bonanos, F. Lenrick, R. Wallenberg, *Journal of Power Sources* **218** (2012) 313.

[19]   R. Peng, T. Wu, W. Liu, X. Liu, G. Meng, *Journal of Materials Chemistry* **20** (2010) (30) 6218.

[20]   E. Fabbri, L. Bi, D. Pergolesi, E. Traversa, *Energy & Environmental Science* **4** (2011) (12) 4984.

[21]   C. Solis, L. Navarrete, S. Roitsch, J.M. Serra, *Journal of Materials Chemistry* **22** (2012) (31) 16051.

[22]   L. Navarrete, C. Solis, J.M. Serra, *Journal of Materials Chemistry A* **3** (2015) (32) 16440.

[23]   C. Solis, L. Navarrete, F. Bozza, N. Bonanos, J.M. Serra, *ChemElectroChem* **2** (2015) (8) 1106.

[24]   S.S. Li, R.Q. Yan, G.J. Wu, K. Xie, J.G. Cheng, *International Journal of Hydrogen Energy* **38** (2013) (35) 14943.

[25]   L.Z. Gan, L.T. Ye, M.Z. Liu, S.W. Tao, K. Xie, *Rsc Advances* **6** (2016) (1) 641.

[26]   E. Quarez, K.V. Kravchyk, O. Joubert, *Solid State Ionics* **216** (2012) 19.

[27]   X.G. Cao, S.P. Jiang, *International Journal of Hydrogen Energy* **38** (2013) (5) 2421.

[28]   Y.J. Leng, S.H. Chan, K.A. Khor, S.P. Jiang, *Journal of Solid State Electrochemistry* **10** (2006) (6) 339.

[29]   E.P. Murray, T. Tsai, S.A. Barnett, *Solid State Ionics* **110** (1998) (3–4) 235.

[30]   R. Strandbakke, V.A. Cherepanov, A.Y. Zuev, D.S. Tsvetkov, C. Argirusis, G. Sourkouni, S. Prunte, T. Norby, *Solid State Ionics* **278** (2015) 120.

[31]   R. Strandbakke, E. Vøllestad, S.A. Robinson, M.-L. Fontaine, T. Norby, *Journal of The Electrochemical Society* **164** (2017) (4) F196.

[32]   S. Ricote, N. Bonanos, H.J. Wang, R. Haugsrud, *Solid State Ionics* **185** (2011) (1) 11.